Light absorption enhancement in heterostructure organic solar cells through the integration of 1-D plasmonic gratings

Pierfrancesco Zilio,[1,2,3,*] Davide Sammito,[2,3,4] Gabriele Zacco,[1,2,3] Marco Mazzeo,[5,6] Giuseppe Gigli,[5,6] and Filippo Romanato[1,2,3]

[1]*Department of Physics, Padova University, via Marzolo 8, 35131 Padova, Italy*
[2]*LANN Laboratory for Nanofabrication of Nanodevices, Corso Stati Uniti 4, 35127 Padova, Italy*
[3]*IOM-CNR, TASC National Laboratory, via S.S. 14, Km 163.5 in Area Science Park, 34149 Basovizza (Ts), Italy*
[4]*Trieste University, Piazzale Europa 1, 34127 Trieste, Italy*
[5]*NNL CNR NANO, via Arnesano, 73100 Lecce, Italy*
[6]*Department of Mathematics and Physics "E. De Giorgi", Campus Universitario, via Monteroni, 73100, lecce, Italy*
**pierfrancesco.zilio@venetonanotech.it*

Abstract. The integration of a plasmonic lamellar grating in a heterostructure organic solar cell as a light trapping mechanism is investigated with numerical Finite Elements simulations. A global optimization of all the geometric parameters has been performed. The obtained wide-band enhancement in optical absorption is correlated with both the propagating and the localized plasmonic modes of the structure, which have been identified and characterized in detail.

OCIS codes: (350.6050) Solar energy; (040.5350) Photovoltaic; (250.5403) Plasmonics; (240.6680) Surface plasmons; (050.2770) Gratings.

References and links

1. H. Hoppe and N. S. Sariciftci, "Organic solar cells: an overview," J. Mater. Res. **19**(07), 1924–1945 (2004).
2. T. Kietzke, "Recent advances in organic solar cells," Adv. Optoelectron. **2007**, 40285 (2007).
3. P. E. Shaw, A. Ruseckas, and I. D. W. Samuel, "Exciton diffusion measurements in poly(3-hexylthiophene)," Adv. Mater. (Deerfield Beach Fla.) **20**(18), 3516–3520 (2008).
4. L. Tsakalakos, "Nanostructures for photovoltaics," Mater. Sci. Eng. Rep. **62**(6), 175–189 (2008).
5. H. A. Atwater and A. Polman, "Plasmonics for improved photovoltaic devices," Nat. Mater. **9**(3), 205–213 (2010).
6. R. B. Dunbar, T. Pfadler, and L. Schmidt-Mende, "Highly absorbing solar cells--a survey of plasmonic nanostructures," Opt. Express **20**(S2 Suppl 2), A177–A189 (2012).
7. V. E. Ferry, J. N. Munday, and H. A. Atwater, "Design considerations for plasmonic photovoltaics," Adv. Mater. (Deerfield Beach Fla.) **22**(43), 4794–4808 (2010).
8. M. Agrawal and P. Peumans, "Broadband optical absorption enhancement through coherent light trapping in thin-film photovoltaic cells," Opt. Express **16**(8), 5385–5396 (2008).
9. P. Spinelli, M. Hebbink, R. de Waele, L. Black, F. Lenzmann, and A. Polman, "Optical impedance matching using coupled plasmonic nanoparticle arrays," Nano Lett. **11**(4), 1760–1765 (2011).
10. J. N. Munday and H. A. Atwater, "Large integrated absorption enhancement in plasmonic solar cells by combining metallic gratings and antireflection coatings," Nano Lett. **11**(6), 2195–2201 (2011).
11. R. A. Pala, J. White, E. Barnard, J. Liu, and M. L. Brongersma, "Design of plasmonic thin-film solar cells with broadband absorption enhancements," Adv. Mater. (Deerfield Beach Fla.) **21**(34), 3504–3509 (2009).
12. M. G. Kang, T. Xu, H. J. Park, X. Luo, and L. J. Guo, "Efficiency enhancement of organic solar cells using transparent plasmonic Ag nanowires electrodes," Adv. Mater. (Deerfield Beach Fla.) **22**(39), 4378–4383 (2010).
13. K. Q. Le, A. Abass, B. Maes, P. Bienstman, and A. Alù, "Comparing plasmonic and dielectric gratings for absorption enhancement in thin-film organic solar cells," Opt. Express **20**(S1), A39–A50 (2012).
14. C. Min, J. Li, G. Veronis, J. Y. Lee, S. Fan, and P. Peumans, "Enhancement of optical absorption in thin-film organic solar cells trough the excitation of plasmonic modes in metallic gratings," Appl. Phys. Lett. **96**(13), 133302 (2010).
15. H. Shen and B. Maes, "Combined plasmonic gratings in organic solar cells," Opt. Express **19**(S6 Suppl 6), A1202–A1210 (2011).
16. A. J. Morfa, K. L. Rowlen, T. H. Reilly, M. J. Romero, and J. van de Lagemaat, "Plasmon-enhanced solar energy conversion in organic bulk heterojunction photovoltaics," Appl. Phys. Lett. **92**(1), 013504 (2008).

#162303 - $15.00 USD Received 15 Feb 2012; revised 13 Apr 2012; accepted 19 Apr 2012; published 15 May 2012

17. S. A. Maier, *Plasmonics Fundamentals and Applications* (Springer 2007).
18. K. Walzer, B. Maennig, M. Pfeiffer, and K. Leo, "Highly efficient organic devices based on electrically doped transport layers," Chem. Rev. **107**(4), 1233–1271 (2007).
19. M. Mazzeo, F. della Sala, F. Mariano, G. Melcarne, S. D' Agostino, Y. Duan, R. Cingolani, and G. Gigli, "Shaping white light through electroluminescent fully organic coupled microcavities," Adv. Mater. (Deerfield Beach Fla.) **22**(42), 4696–4700 (2010).
20. E. D. Palik, *Handbook of Optical Constants of Solids* (Elsevier, 1998).
21. Comsol Multiphysics, http://www.comsol.com.
22. J. M. Jin, *The Finite Element Method in Electromagnetics*, 2nd ed. (Wiley & Sons, 2002).
23. S. I. Bozhevolnyi and T. Søndergaard, "General properties of slow-plasmon resonant nanostructures: nano-antennas and resonators," Opt. Express **15**(17), 10869–10877 (2007).
24. E. S. Barnard, J. S. White, A. Chandran, and M. L. Brongersma, "Spectral properties of plasmonic resonator antennas," Opt. Express **16**(21), 16529–16537 (2008).
25. R. Gordon, "Light in a subwavelength slit in a metal: propagation and reflection," Phys. Rev. B **73**(15), 153405 (2006).

1. Introduction

Organic semiconductors are excellent absorbers of EM radiation but have poor electrical properties [1,2]. Due to the limited diffusion length of the excitons photogenerated in the absorbing layers, the physical thickness of organic solar cells (OSC) is limited to few tens of nanometers [3]. Thus the realization of light trapping systems is mandatory in combination with such ultra-thin solar cells in order to get significant values of conversion efficiency. Among the possible approaches to light trapping [4], plasmonic nanostructures are acquiring more and more interest in the scientific community due to their capability to confine the optical energy in subwavelength extended regions [5–16].

Plasmonic light trapping systems offer two main mechanisms to concentrate light, Localized Surface Plasmons (LSPs) and Surface Plasmon Polaritons (SPPs) [17]. The first resonances are characteristic of small metal nanoparticles and yield very high field enhancement within a few nanometers from the metal surface. In combination with ultra-thin absorber layers, nanoparticles size is designed to make the absorption cross section overwhelming compared to the relative scattering cross section [5]. On the other hand, SPPs are evanescent waves propagating at a metal-dielectric interface which provide lower field concentrations within a higher range, usually around 100 nm. As well known [17], light travelling in a dielectric medium cannot directly couple to a SPP mode at the flat interface due to a momentum mismatch. Coupling is possible by means of properly designed nanostructured gratings, in order to transfer the power of impinging light to surface waves.

Several works in literature already considered the integration of plasmonic crystals as light trapping mechanism in both inorganic [10,11] and organic [12–16] photovoltaic devices. In combination with LSP [10–11, 13–16] and SPP [12–15] resonances, periodic arrays of metallic nanostructures can be designed to excite waveguide modes of the structure [10–12] and enhance the optical thickness of the device. Kang et al. [12] have experimentally demonstrated the effectiveness of this approach measuring a 40% increase in short circuit current in an ultra-thin OSC embedding a silver nanowires grating. The aim of our work is to analyze in detail the excitation conditions of localized resonances and propagating modes, both SPP and conventional waveguide modes, supported by a plasmonic crystal integrated in an OSC and to clearly highlight their role in providing the observed absorption enhancement. In fact, in literature, the identification of the different plasmonic modes involved often is performed by only examining the EM field pattern at peak wavelengths [13,14] or not explicitly showing the modal analysis procedure used [12]. Furthermore, unlike many papers, we focused on a realistic heterostructure device layout in which the metallic nanowires are not in contact with the absorber layers in order to reduce the effect of unwanted recombination mechanisms for the photogenerated excitons.

The paper is organized as follows. In Section 2 we present the OSC layout integrating the plasmonic nanostructure considered. Section 3 reports the results of an overall optimization of both the plasmonic nanostructures geometric parameters and of the OSC layers thickness,

#162303 - $15.00 USD Received 15 Feb 2012; revised 13 Apr 2012; accepted 19 Apr 2012; published 15 May 2012

showing that a relevant enhancement can be obtained. Sections 4, 5 and 6 are devoted to identify in detail the origins of the observed enhanced absorption, correlating the different spectral enhancement peaks with plasmonic resonances. This is done investigating first the optical eigenmodes of the flat configurations (without any gratings or in presence of a 10 nm uniform silver metal film, Section 4) and then the resonances of a single plasmonic nanostrip placed within the OSC stack (Section 5). Finally, in Section 6, we consider the whole plasmonic grating, providing evidence that it supports both localized and propagating resonances. Both of them play a role in the overall spectral enhancement and give rise to an effective light trapping mechanism.

2. Plasmonic OSC model

We considered the solar cell layout with the schematic cross section shown in Fig. 1(a). A 3D view of the cell is reported in Fig. 1(b). It is a p-i-n cell in superstrate configuration with a central heterojunction whose active layer is made of a Copper Phthalocyanine (CuPc, 20 nm) - Fullerene (C60, 10 nm) bilayer. The absorbers are embedded between the Hole Transport Layer (HTL), made of N′,N′-tetrakis(4-methoxyphenyl)-benzidine (Meo-TPD) doped with 2,3,5,6-tetrafluoro-7,7,8,8,-tetracyanoquinodimethane (F4-TCNQ), and the Electron Transport Layer (ETL), which is constituted by Rhodamine B doped fullerene (C60:RhB). The p-i-n configuration is chosen since the modification of transport layers thickness does not strongly affect the electrical properties thus allowing the optimization of the vertical photonic structure of the cell [18,19]. A 1D silver grating with square wave profile is embedded in the HTL (see Fig. 1). The refractive index dispersion relations for organic layers, ITO (120 nm thick) and glass were extracted with ellipsometric measurements while those for the metals were taken from Palik's Handbook of Optical Constants [20]. We used the software Comsol Multiphysics [21] to perform 2D Finite Elements optical simulations of the EM field distribution for the three variations of the basic device layout mentioned before (full grating, flat and isolated strip).

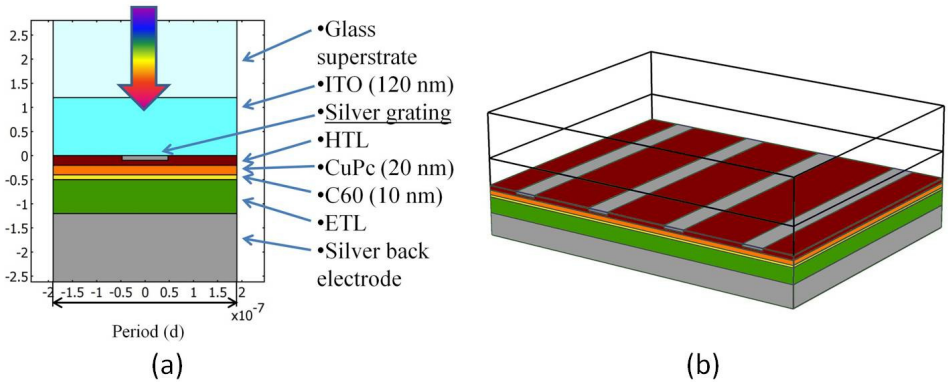

Fig. 1. 2D FEM model cross section (a) and 3D picture (b) of the plasmonic OSC.

3. Grating parameters optimization

In the full grating structure FEM model (Fig. 1(a)), periodic boundary conditions are set at the lateral boundaries of the unit cell, while at the upper and lower sides of the model Perfectly Matched Layers (PMLs) [22] simulate an infinite extension of air and silver respectively (not shown in Fig. 1(a)). TE and TM polarized normally impinging monochromatic plane waves with unitary power are set as illumination. For both polarizations we calculated the reflectance (R), through the Poynting vector flux at the top boundary, and the absorptance (Q). The latter is the fraction of incident power absorbed in the organic layers and it is computed as the integral over the corresponding domains of the

#162303 - $15.00 USD Received 15 Feb 2012; revised 13 Apr 2012; accepted 19 Apr 2012; published 15 May 2012

quantity $\frac{1}{2}\omega \mathrm{Im}(\varepsilon)|E|^2$, where ω is the impinging radiation frequency, ε is the organic layers dielectric constant and E is the electric field. To evaluate the absorption performance of the cell we defined a figure of merit called Throughput (T):

$$T = \frac{\int Q(\lambda)F(\lambda)d\lambda}{\int F(\lambda)d\lambda} \quad (1)$$

with F being the *AM1.5* solar photon flux. We considered the wavelength range between 300 and 1100 nm within which the absorption of the CuPc-C60 bilayer is appreciable (see Fig. 2(c)).

We modeled both the layouts with and without the grating. In the optimization of the cell geometry we simultaneously varied the grating parameters and the thickness of ETL and HTL. We tuned the transport layers thicknesses in a range from 20 to 70 nm in order to not affect the electrical properties of the cell [18]. In the case of the cell without grating, we found that the optimal thicknesses of the spacer layers are 30 nm and 60 nm respectively for HTL and ETL. For the plasmonic device, the grating geometry that maximizes the throughput has a period of 380 nm, a thickness of 10 nm and a strip width-to-period ratio of 25% (Ag width of 95 nm) whereas HTL and ETL optimal thicknesses are 20 nm and 70 nm respectively.

Figure 2(a) reports the absorption spectra within active layers (Q) and within metal domains (Q_m) and the reflectance spectra (R) in the optimal cell with plasmonic grating compared to the optimal cell layout without grating. It is evident that a wide enhancement band is found in the wavelength range from 480 nm to 1100 nm. The overall throughput enhancement reached by the optimal grating configuration compared to the best flat reference configuration is + 11.8% (−1.8% for 300 nm < λ < 480 nm, + 12.5% for 480 nm < λ < 900 nm, + 1.1% for 900 nm < λ < 1100 nm). In the device integrating the plasmonic crystal an increased metal dissipation is found for λ > 600 nm while the reduced organic layers absorption in the UV is due to an increase in reflectivity. Despite introducing these losses, the grating improves the absorption in the device otherwise limited by the low thickness of the active layers and the resulting high reflectivity.

The spectral amount of absorption enhancement for the two orthogonal polarizations TM and TE (respectively magnetic and electric field parallel to the silver strips) is reported in Fig. 2(b). As can be expected from an anisotropic structure such as a 1D grating, a strong polarization dependence of the enhancement is found. The TM contribution to the overall throughput enhancement is + 20.3%, while the TE one is + 3.2%. Looking at the TM spectrum, in particular, two broad enhancement peaks are observed at λ = 780 nm and λ = 1100 nm. However the long wavelength peak contribution to throughput enhancement is really limited due to the low Q absolute value. Also the TE spectrum presents a band of enhancement, although it is more modest with respect to TM polarization and it drops below unity in the outer regions of the considered wavelength range. It is worth noting that both the TE and TM enhancements fall within the maximum absorption spectral window of CuPc (see Fig. 2(c)). The FEM studies performed in what follows are aimed to get a clear understanding of the reasons of the observed enhancement.

#162303 - $15.00 USD Received 15 Feb 2012; revised 13 Apr 2012; accepted 19 Apr 2012; published 15 May 2012

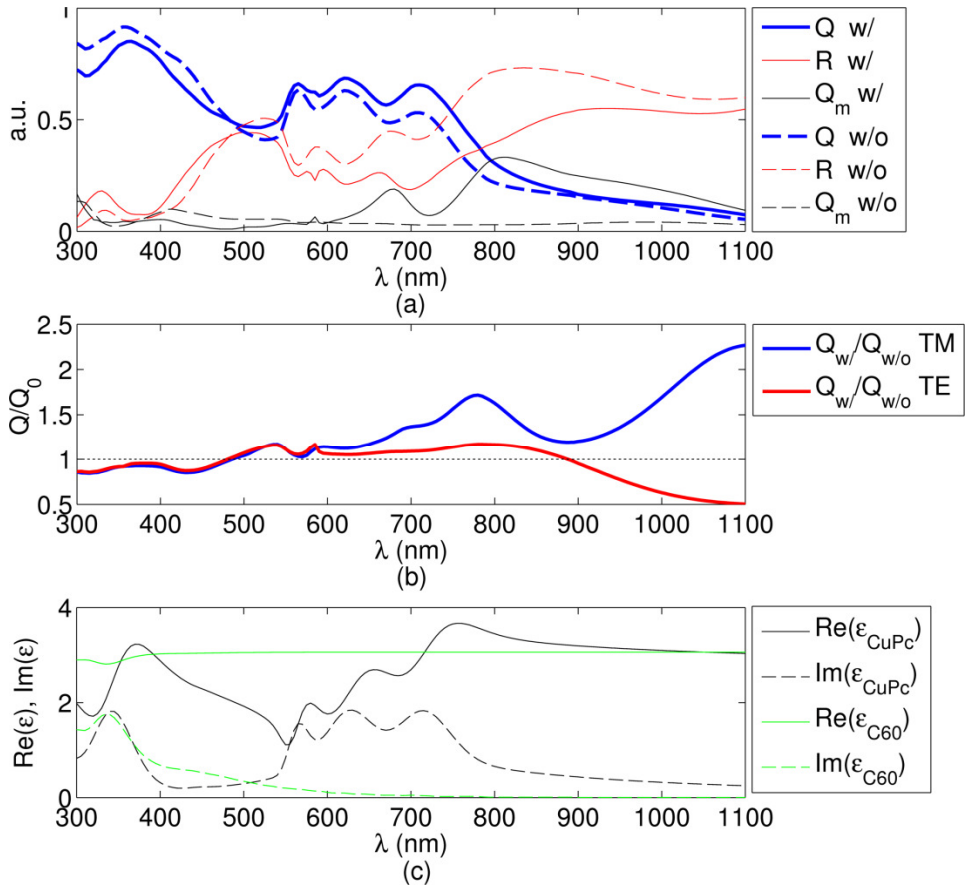

Fig. 2. (a) Absorptance within active layers CuPc and C60 (blue solid line), absorptance in metal parts (black solid line) and reflectance (red solid line) of the optimal cell compared to the same quantities calculated for the optimal cell without grating (dashed lines); (b) Absorptance enhancement (Q/Q_0) in the active layers for TM (blue) and TE (red) polarizations; (c) Real and Imaginary parts of relative dielectric constants of CuPc (black) and of C60 (green).

4. Modal analysis of the flat configurations

The main function of the grating is to couple incident light into the guided modes of the multilayer stack constituting the OSC [10–15]. In order to clearly identify which are the possible photonic and plasmonic modes we performed a modal analysis of the structure by means of FEM simulations in case of absence of any grating and with a continuous 10 nm silver film in place of the grating. The real parts of the obtained TM optical modes dispersions are reported in Fig. 3 while the respective mode electric field norm profiles at some representative frequencies are reported in Fig. 4.

The basic TM guided modes of the structure in absence of any grating (red curves in Fig. 3) are two: a Surface Plasmon Polariton mode at the interface between the back silver contact and the ETL organic layer and a TM_0 waveguide mode within the ITO slab (respectively Fig. 4(a) and 4(b), red curves). The former, in particular, allows a high field enhancement within the organic layers. The structure with 10 nm continuous Silver layer also sustains these modes (see corresponding black lines in Fig. 3). In particular, the SPP dispersion remains similar to that one obtained in absence of the top Ag film. Nevertheless, while at high frequencies the field is mostly confined close to the back electrode (Fig. 4(a) green curve) at

#162303 - $15.00 USD Received 15 Feb 2012; revised 13 Apr 2012; accepted 19 Apr 2012; published 15 May 2012

lower frequencies it results much more concentrated within the ITO layer in the case of presence of Ag film (Fig. 4(a), black field profile).

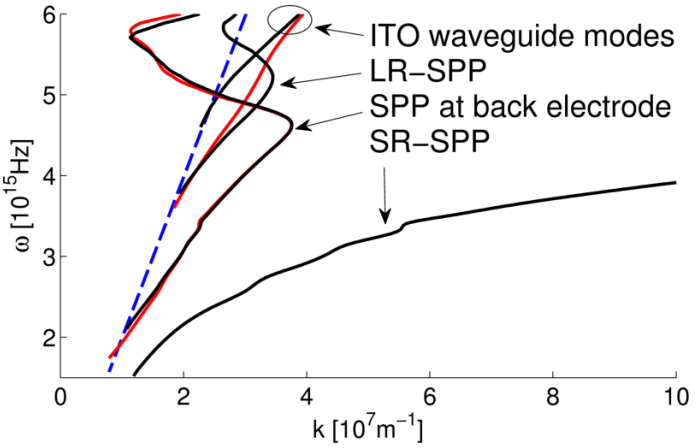

Fig. 3. TM Modes dispersion for flat configurations with (black) and without (red) 10 nm continuous Ag film between the ITO layer and the HTL. The blue dashed line is the light line in glass.

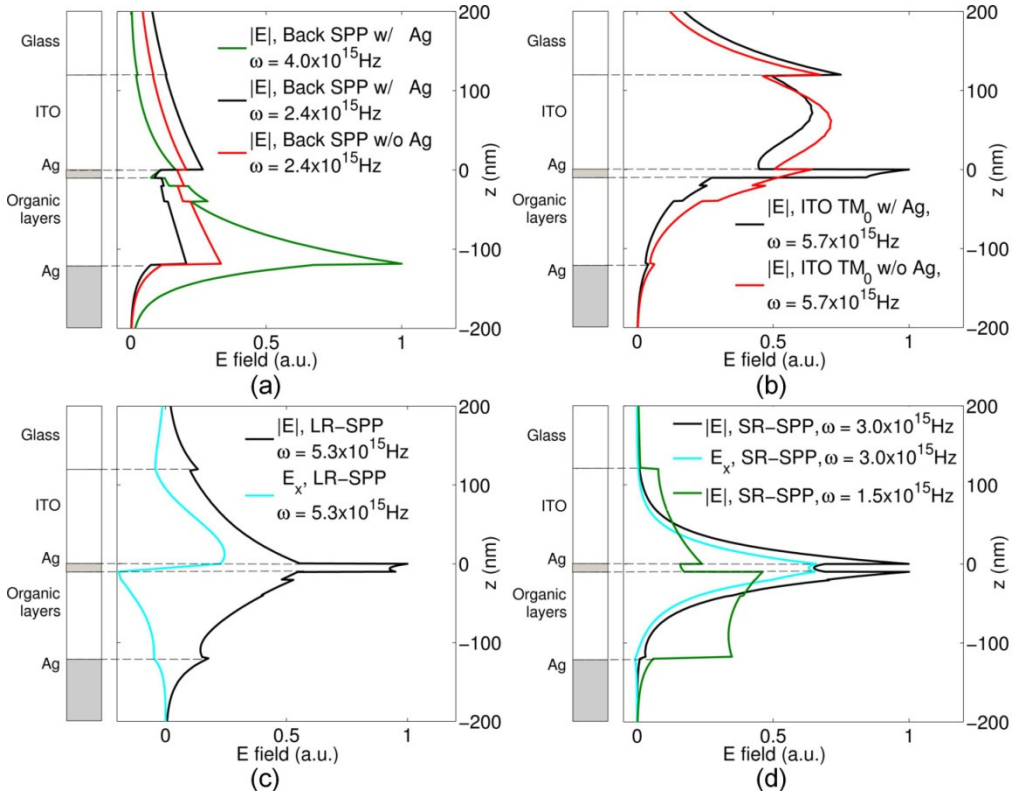

Fig. 4. Electric field profiles of modes at representative frequencies. (a) back electrode SPP modes with and without 10 nm Ag film; (b) TM_0 ITO waveguide modes with and without 10 nm Ag film; (c) LR-SPP mode; (d) SR-SPP mode.

The structure with the Ag film sustains two more guided modes, a Long Range SPP mode (LR-SPP) and a Short Range SPP mode (SR-SPP) [17], which can be identified from

#162303 - $15.00 USD Received 15 Feb 2012; revised 13 Apr 2012; accepted 19 Apr 2012; published 15 May 2012

symmetry considerations on the electric field component along the film interface (respectively antisymmetric and symmetric, see Fig. 4(c), 4(d), cyan curves).

It is interesting to analyze the frequency behavior of the SR-SPP mode field profile (Fig. 4(d)). While at high frequencies (~$3\cdot10^{15}$ Hz, black curve) the field profile is highly concentrated close to the metal layer, at lower frequencies (~$1.5\cdot10^{15}$ Hz, green curve) the mode is much more delocalized and produces an almost uniform field enhancement within the whole organic layer slab. The mode changes its nature and becomes much more similar to a metal-dielectric-metal plasmonic mode [17].

5. Single strip resonance study

The resonant features of a *single* isolated silver strip embedded in the HTL were investigated by means of a scattering 2D FEM model. The scattering simulation goes through two steps. First we calculate the background Electric field $\boldsymbol{E_b}$ given by a TM-polarized monochromatic plane wave normally impinging on the OSC model without any plasmonic structures. Then the wave equation is solved for the scattering field $\boldsymbol{E}_s$ in presence of the single metal strip, assuming the full field is given by $\boldsymbol{E}_{tot} = \boldsymbol{E}_b + \boldsymbol{E}_s$ [21,22]. PMLs are placed at all the outer boundaries in order to simulate an infinite space extension around the strip (Fig. 5(b), 5(c)). In Fig. 5(a) we report the map of normalized absorption cross section of the strip, calculated as the absorption within the strip divided by the strip width times the light power incident on the strip cross section.

We find out that characteristic absorption regions visible in Fig. 5(a) are related to the resonant behavior of Short Range SPP travelling back and forth on the strip in the horizontal direction, according to a simple Fabry-Perot resonator model [23,24]:

$$w \cdot k_{SR-SPP}(\omega) = m\pi + \phi \qquad (2)$$

where w is the strip width, $k_{SR\text{-}SPP}(\omega)$ is the momentum of the SR-SPP mode, m is an integer number and ϕ is the proper phase pickup upon reflection at the strip ends. As pointed out in [23–25], ϕ in general depends on frequency but the variation is slow for a high magnitude of the real part of the relative permittivity of the metal (over 10). This condition is satisfied for silver at frequencies lower than about $3.5\cdot10^{15}$ Hz. So, as a first order approximation, we consider ϕ to be a constant. Inserting the SR-SPP mode momentum calculated for a continuous film in previous section inside Eq. (2) and solving the equation numerically, we find the optimal ϕ in order to have good agreement between the model and scattering FEM simulation. The best fit, $\phi \approx 1.2$ rad, is comparable to phase pickup values obtained by ab initio calculations in similar studies [23,24] for strips much thinner than free space wavelength. In Fig. 5(a) black lines are the solutions of Eq. (2) for different values for m. In particular, for symmetry reasons, only the odd modes (m = 1,3,5…) can be excited in the considered top illumination geometry. As is seen, the Fabry-Perot resonator model correctly individuates the locations of the strip absorption maxima.

As can also be seen from the map, for the strip width of the optimal grating configuration determined in Section 3, w = 95 nm, a single strip resonance is expected in a broad frequency band ranging from 1.8 to $2.7\cdot10^{15}$ Hz. The presence of single strip resonances in the optical response of the grating is reasonable since the separation between the strips in the optimal configuration is pretty high (285 nm) and highly localized resonances are therefore expected to be unaffected by grating periodicity.

Figures 5(b), 5(c) report two scattered electric field norm distributions sampled along the single strip resonance (circles in Fig. 5(a)). The field appears to be much more delocalized at low frequency (Fig. 5(b)) than at high frequency (Fig. 5(c)). This is in agreement with the frequency dependence of the SR-SPP mode field profile discussed in previous section.

#162303 - $15.00 USD Received 15 Feb 2012; revised 13 Apr 2012; accepted 19 Apr 2012; published 15 May 2012

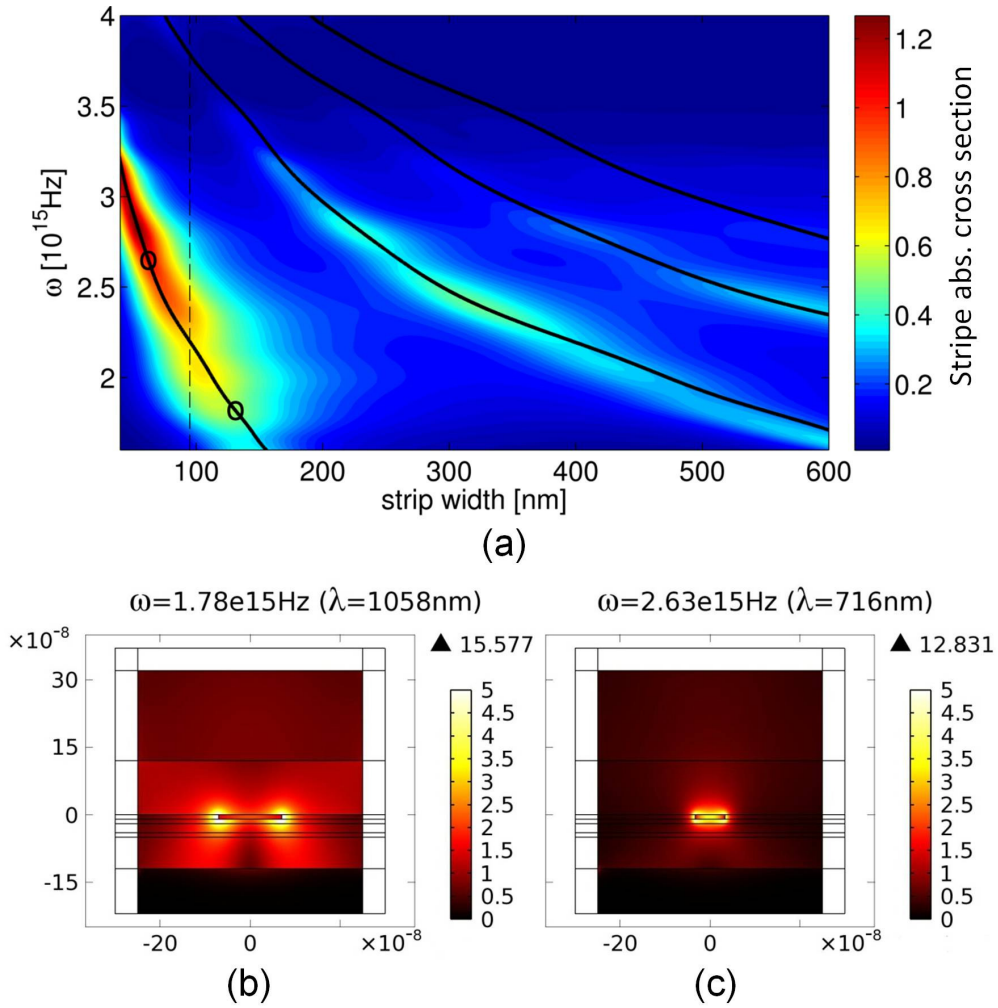

Fig. 5. (a) Single strip normalized absorption cross section as a function of strip width and frequency. Black solid lines mark single strip resonance positions according to Eq. (2) with $\phi \approx 1.2$ rad; the vertical dashed line mark the optimal strip width configuration as found in Section 3; (b), (c): Scattered electric field norms in the configurations marked with circles in the map; their strip widths are respectively 140 and 66 nm. Color scales in (b), (c) are normalized to the impinging wave electric field norm.

6. Full plasmonic grating structure study

Once identified the modes and resonances supported in the structure, we want to highlight the role of the grating in exciting such field configurations and the role of localized and propagating surface plasmons in increasing the cell absorption.

#162303 - $15.00 USD Received 15 Feb 2012; revised 13 Apr 2012; accepted 19 Apr 2012; published 15 May 2012

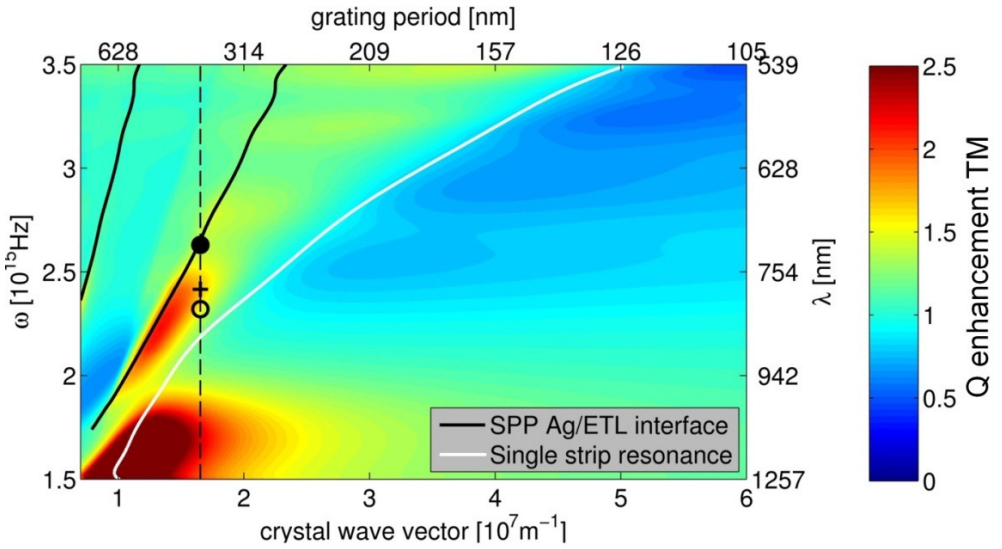

Fig. 6. TM Absorption enhancement within the organic layers with respect to the optimal cell without any grating as a function of crystal wave vector G = 2π/d and angular frequency ω. Black lines are the back SPP coupling dispersions according to Eq. (3) for m = 1, 2, while the white line represents the single strip resonance, i.e. the zero of Eq. (2) for m = 1. The optimal grating period is marked with the dashed black line. Empty and filled circles mark configurations whose electric field norm is reported respectively in Fig. 8(a) and 8(b); the "+" marks the peak of absorption enhancement at λ = 780 nm.

We start considering the TM polarization, which plays the major role in determining the light trapping properties. In Fig. 6 we report the map of absorption enhancement within the organic layers with respect to the optimized cell without any grating, in the case of TM polarized impinging light. This map, as well as the following ones, are calculated assuming grating thickness and strip width-to-period ratio fixed to the optimal values of 10nm and 25% respectively, and letting the grating wave vector $G = 2\pi/d$ vary. The optimal grating wave vector obtained in Section 3 is here marked by the dashed line. Note that keeping the strip-to-period ratio fixed has the advantage to avoid the bias that would appear keeping the strip width fixed, i.e. small-period configurations would unavoidably present lower enhancements with respect to higher ones, due to the higher fraction of cell surface covered by the metal strips.

In Fig. 6 two evident high-enhancement regions are present, one in the range 700 nm < λ < 900 nm, the other in the IR part of the spectrum. As was discussed in Section 3, the former region provides the main contribution to the overall throughput enhancement since it partially overlaps to the band of maximal absorption of CuPc layer. The latter region, although shows a much greater absorption enhancement (the maximum value reached, a factor 11, is out of the color scale) contributes to a much lower extent to the throughput.

Two basic plasmonic mechanisms contribute to the enhancements found. One of them is directly related to the dispersion $k_{SPP}(\omega)$ of the SPP at the back electrode/ETL interface which was numerically found in Section 4 analyzing the flat configurations. The grating works as a plasmon coupler, allowing the incident radiation to couple to the flat back electrode SPP mode, according to the well known relation [17]

$$mG = m\frac{2\pi}{d} = k_{SPP}(\omega) \qquad m = \pm 1, \pm 2, \pm 3, \ldots \tag{3}$$

#162303 - $15.00 USD Received 15 Feb 2012; revised 13 Apr 2012; accepted 19 Apr 2012; published 15 May 2012

This is clearly seen superimposing to the map the curves given by (k, ω) = ($m^{-1}\cdot k_{SPP}(\omega)$, ω), (black curves in Fig. 6 and in following maps). The curve corresponding to m = 1 approximately follows the relevant enhancement region found at ω > $2\cdot10^{15}$ Hz (λ < 940 nm).

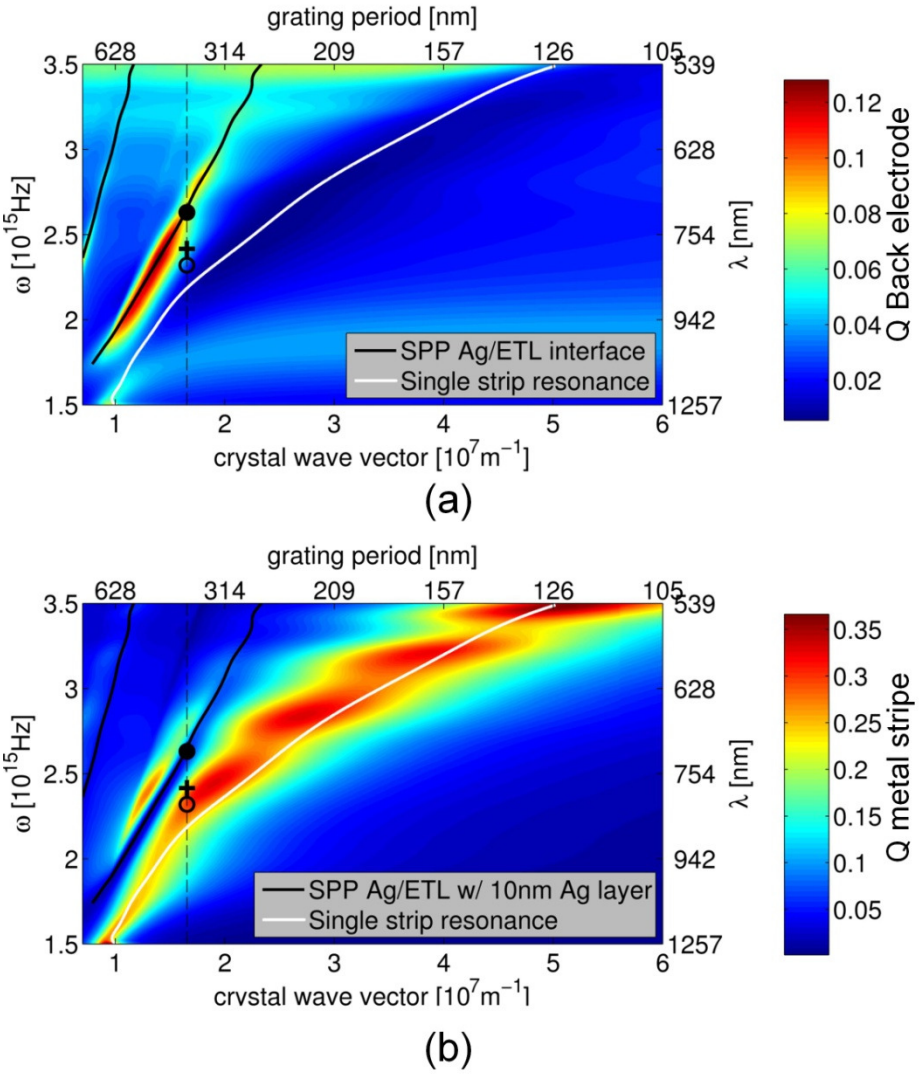

Fig. 7. TM Absorptance in back electrode (a) and in the metal strips (b) as a function of crystal wave vector G = 2π/d and angular frequency ω. Strip-width-to-period ratio and grating thickness are kept fixed to 25% and 10 nm respectively. In both maps the black lines are the back SPP coupling dispersions according to Eq. (3) for m = 1, 2, while the white line represents the single strip resonance, i.e. the zero of Eq. (2) for m = 1. The vertical black dotted line marks the optimal grating period (380 nm). Filled and empty circles mark the configurations whose electric field norm is reported in Fig. 8(a) and 8(b).

Further evidence of this coupling mechanism is obtained superimposing the same curves to a map of losses within the back electrode for TM polarization as a function of G and ω (Fig. 7(a)). SPPs at back electrode, when present, are expected to strongly increase metal losses, beside absorption in the organic layers. As a matter of fact, high dissipation regions are found in Fig. 7(a) exactly along black curves. Incidentally, in this map we note also a

#162303 - $15.00 USD Received 15 Feb 2012; revised 13 Apr 2012; accepted 19 Apr 2012; published 15 May 2012

weak absorption region between 1.5 and $2\cdot10^{15}$ Hz which is almost constant for G > $2\cdot10^{7}\mathrm{m}^{-1}$. This corresponds to a vertical resonance of the flat multilayer structure.

The second basic plasmonic mechanism is related to the single strip SPP resonance described in Section 5. This is marked with a white line in all the presented maps. The line is obtained from Eq. (2) assuming the same constant value for the SR-SPP reflection phase ϕ, as discussed in the previous section. Note that, since we keep the strip-to-period ratio fixed, the strip width varies with period in the map and, as a result, the resonance location disperses with period. As is seen in Fig. 6, the white line individuates the location of the maximal enhancement in the IR and also approximately follows the high-enhancement region in the range 700 nm < λ < 900 nm.

The presence this resonance becomes more evident analyzing the map of absorptance in the strips of the grating as a function of G and ω (Fig. 7(b)). Here a strong dissipation feature is visible spanning the entire map. As is seen, it is well fitted by the single strip resonance curve. The back SPP couplings (black lines) correspond instead to narrow strip absorption minima. This is expected, since in these configurations most of the EM energy is localized close to the back electrode.

In Fig. 8 we report the electric field norm distributions of the configuration marked with circles in Figs. 6 and 7. Figure 8(a) corresponds to the empty circle, which is taken at the optimal period at the frequency corresponding to a maximum dissipation in the strips (ω = $2.32\cdot10^{15}$ Hz, λ = 812 nm). Figure 8(b) corresponds to the filled circle in the maps, which is taken along the the m = 1 back-SPP coupling region (ω = $2.63\cdot10^{15}$ Hz, λ = 716 nm). In the former case, the field is mostly confined close to the metal strip and is actually similar to the field reported in Fig. 5(b), 5(c) for the case of isolated strips. In Fig. 8(b), instead, a clear SPP field pattern at back electrode is visible. The field distributions are therefore coherent with the interpretation of resonances given above.

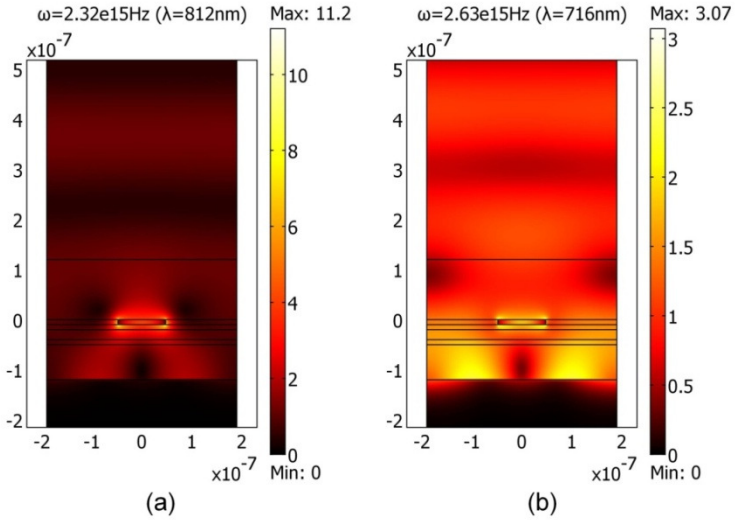

Fig. 8. Electric field norm for configurations marked with an empty circle (a) and with a filled circle (b) in Fig. 6 and 7 and corresponding respectively to the single strip resonance and to the SPP at back electrode coupling. Frequencies are respectively ω = $2.32\cdot10^{15}$ Hz and $2.63\cdot10^{15}$ Hz. Geometrical parameters are those of the optimal configuration. Colorscale is normalized to the impinging wave electric field norm.

Looking at Fig. 6, it has to be noticed that the peak of absorption enhancement in the optimal configuration at λ = 780 nm (marked with a cross) lies between the single strip and the back-SPP resonances. We conclude that, actually, the overall enhancement in that spectral region is due to a combination of the two resonances. This is supported also by the

#162303 - $15.00 USD Received 15 Feb 2012; revised 13 Apr 2012; accepted 19 Apr 2012; published 15 May 2012

field maps in Fig. 8. Both of them show an enhanced concentration of the electric field in correspondence of the active layers.

The enhancement region in the IR part of the spectrum, instead, is mainly related to the single strip resonance. As discussed in Section 4 and 5, the SR-SPP mode with decreasing frequency gradually turns into a metal-dielectric-metal plasmonic mode, and its electric field overlaps the active layers to a greater extent. This determines the progressive increase in the absorption enhancement with decreasing frequency along the single strip resonance, which is clearly seen in Fig. 6. Furthermore, in the IR range the resonance is quite blunt, as can also be seen from the strip-width extension of the feature in the single strip absorption map of Fig. 5(a). For this reason the effect of the single strip resonance is evident in the organic layer absorption spectrum even for strip dimension far from the resonant value.

The TE part of the spectrum, as can be expected from a 1D geometry, contributes to a much lesser extent to the enhancement of absorption within this ultra-thin cell, since it cannot couple to SPP modes [17]. In Fig. 9(a) the TE absorption enhancement within the organic layers is reported as a function of G and ω. As can be noticed, the enhancement region found in Section 3 shows almost no dependence on the period and therefore it is not related to any coupling to TE guided modes of the structure. The strips simply act as non-resonant scatterers of the impinging light, incrementing to a little extent the optical path length. This can be seen looking at the scattered field norm reported in Fig. 9(b) (its configuration is marked with a square in the map). The further sharp enhancement regions in Fig. 9(a) follow the Wood-Rayleigh's anomalies up to frequencies of about $3.5 \cdot 10^{15}$ Hz (λ ~540 nm). These features occur at frequencies corresponding to a change in the number of allowed diffracted orders propagating in the glass substrate, according to the relation

$$G = \frac{\omega \mathrm{Re}(N)}{mc} \quad m = \pm 1, \pm 2, \pm 3, \ldots \tag{4}$$

being N the glass refractive index, c the speed of light, and G the grating momentum. At higher frequencies the TE_0 waveguide modes in the ITO slab become excitable. Their dispersion is shown in Fig. 9 with black lines.

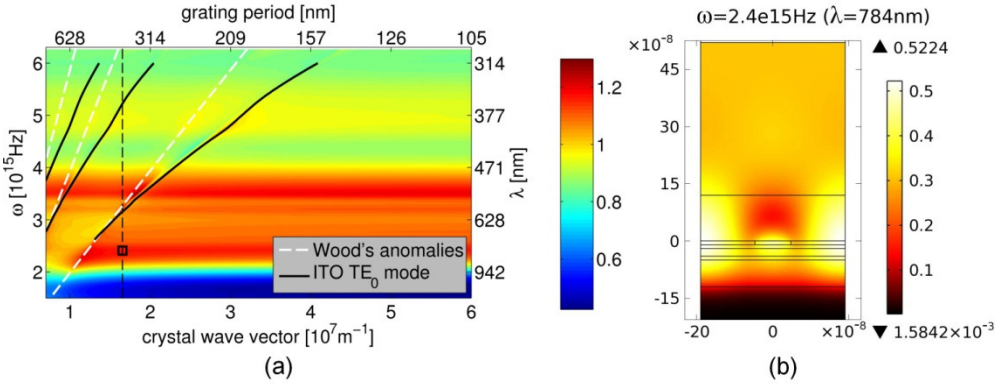

Fig. 9. (a) TE absorption enhancement within the organic layers as a function of $G = 2\pi/d$ and ω; white dashed lines and black lines are Wood's anomalies and ITO TE_0 waveguide modes respectively; the black dashed line marks the optimal grating period; (b) scattered field norm in the configuration marked with a square in the map.

7. Conclusions

Summarizing, we investigated the integration of a thin 1D silver plasmonic grating within a realistic heterostructure organic solar cell. A global optimization of the geometry of the structure has been performed. The obtained throughput enhancement (+ 11.8%) has been

#162303 - $15.00 USD Received 15 Feb 2012; revised 13 Apr 2012; accepted 19 Apr 2012; published 15 May 2012

demonstrated to be largely correlated to the two main plasmonic resonances of the layout for TM polarization, propagating and localized surface plasmon resonances. As a matter of fact, in different frequency ranges, the silver nanostrips constituting the grating are able to couple impinging light to the SPP modes propagating at the back contact surface and behave like single resonant nano-antennas. A contribution of lower importance to the increased device absorption comes from the nanostructures non-resonant scattering of radiation for TE polarization. The combination of these effects leads to a broad-band enhancement extending from 480 nm to beyond 1100 nm.

Acknowledgments

This work has been supported by the University of Padova, by the Ministry of University and Research and by the CARIPARO Foundation, SPLENDID project (Surface PLasmonics for Enhanced Nano-Detectors and Innovative Devices).

#162303 - $15.00 USD Received 15 Feb 2012; revised 13 Apr 2012; accepted 19 Apr 2012; published 15 May 2012